Stochastic analysis of tsunami runup due to heterogeneous coseismic slip and dispersion

F. Løvholt,[1,2,3] G. Pedersen,[2,3] S. Bazin,[1,3] D. Kühn,[3,4] R. E. Bredesen,[5] and C. Harbitz[1,2,3]

[1]   Most tsunami models apply dislocation models that assume uniform slip over the entire fault plane, followed by standard analytical models based on Volterra's theory of elastic dislocations for the seabed deformation. In contrast, we quantify tsunami runup variability for an earthquake with fixed magnitude but with heterogeneous rupture distribution assuming plane wave propagation (i.e., an infinitely long rupture). A simple stochastic analysis of 500 slip realizations illustrates the expected variability in coseismic slip along a fault plane and the subsequent runup that occurs along a coastline in the near field. Because of the need for systematically analyzing different fault geometries, grid resolutions, and hydrodynamic models, several hundred thousand model runs are required. Thus, simple but efficient linear models for the tsunami generation, propagation, and runup estimation are used. The mean value and variability of the maximum runup is identified for a given coastal slope configuration and is analyzed for different dip angles. On the basis of the ensemble runs, nonhydrostatic effects are discussed with respect to their impact on generation, nearshore propagation, and runup. We conclude that for the geometry and magnitude investigated, nonhydrostatic effects reduce the variability of the runup; that is, hydrostatic models will produce an artificially high variability.

Citation: Løvholt, F., G. Pedersen, S. Bazin, D. Kühn, R. E. Bredesen, and C. Harbitz (2012), Stochastic analysis of tsunami runup due to heterogeneous coseismic slip and dispersion, *J. Geophys. Res.*, *117*, C03047, doi:10.1029/2011JC007616.

1. Introduction

[2]   This study is motivated by the need for a quantification of expected variability in runup for a subduction earthquake of given magnitude and mean slip. Tsunami runup prediction has for a long time been based on homogeneous slip distributions of rupture on the fault. Using empirical relationships relating earthquake slip to its magnitude [*Wells and Coppersmith*, 1994; *Henry and Das*, 2001; *Blaser et al.*, 2010; *Leonard*, 2010], one can therefore simply compute the profile of the initial waveform. Modern teleseismic and geodetic inversion techniques however, have shown that the assumption of a uniform slip over the entire rupture plane is invalid. Although several studies have addressed tsunami generation by heterogeneous slip with a relatively complex rupture pattern, it is often in the context of hindcasting past events [e.g., *Wang and Liu*, 2006; *Løvholt et al.*, 2006]. In the present paper, we analyze how heterogeneous coseismic slip affects the initial water surface elevation and consequently the tsunami runup on the coast for a high number of stochastic slip realizations, thereby addressing also the runup uncertainty. The number of studies including this

effect is limited [e.g., *Geist*, 2002; *McCloskey et al.*, 2007, 2008], but conclusive on the fact that the common deterministic practice understates the complexity of the problem. Papers addressing the variations of mean quantities such as the slip and fault dimensions based on magnitude scaling relations [e.g., *Bolshakova and Nosov*, 2011; *Blaser et al.*, 2011] also emphasize the importance of stochastic runup. Herein we choose to only concentrate on slip variations in the dip direction. The available studies in literature addressing tsunamis due to random slip earthquakes are so far limited to the nearshore wave height, thus not attempting the explicit calculation of the runup. This paper quantifies the runup for an ensemble of plane waves generated by earthquakes with different realizations of heterogeneous slip. Because of the need for systematically analyzing different geometries, grid resolutions, and hydrodynamic models, several hundred thousand model runs are required. Thus, simple but efficient linear models for the tsunami generation, propagation, and runup estimation are employed, and an idealized bathymetry is applied. For the same reason, we limit the analysis to plane wave runup; it is stressed that this study is focusing on the theoretical and fundamental aspects of the tsunami generation and runup rather than attempting a description of any historical event. Opposed to previous studies, the present paper includes an elaborate analysis of dispersive effects originating from short-wave components introduced by the slip heterogeneity. *Geist and Dmowska* [1999] indicate that tsunami water levels associated with slip variations in strike direction are greater than those due to corresponding variations in dip direction. This exemplifies

[1]NGI, Oslo, Norway.
[2]Department of Mathematics, University of Oslo, Oslo, Norway.
[3]International Center for Geohazards, Oslo, Norway.
[4]NORSAR, Kjeller, Norway.
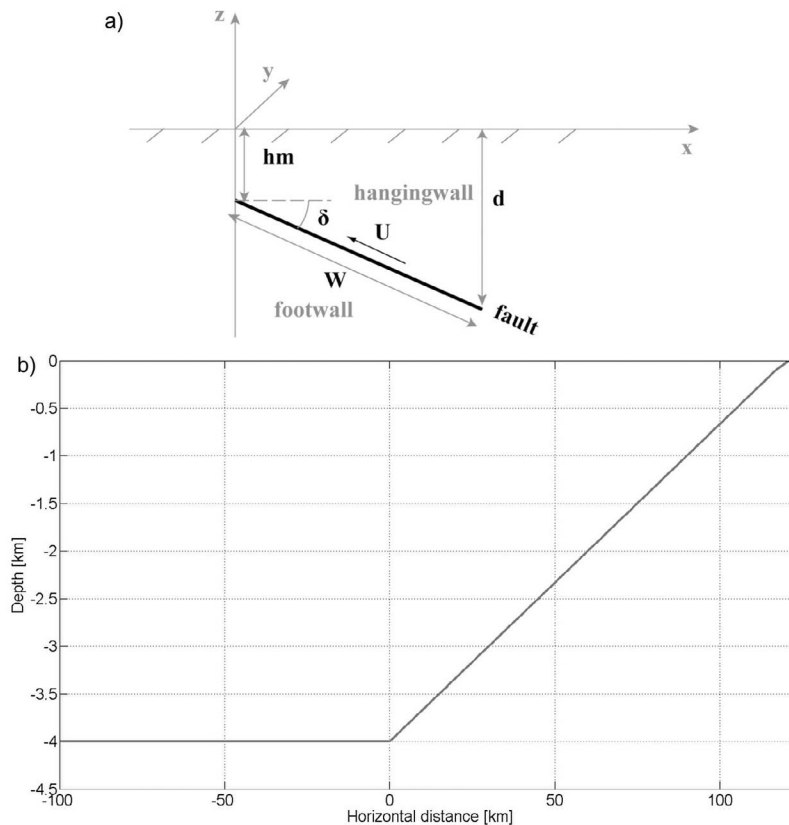[5]Simula Research Laboratory, Lysaker, Norway.

Figure 1. (a) Geometry of the source in the analytical model. The surface displacement due to a rectangular reverse fault in a half-space is computed using the work of *Okada* [1985]. The *y* axis is taken to be parallel to the strike direction of the fault. The *x* axis is taken to be perpendicular to the strike direction of the fault, pointing horizontally in the downdip direction. The *z* axis corresponds to the vertical direction pointing upward from the seabed; δ is the dip angle of the fault plane, and h_m is its shallowest depth below the seabed. W is the width of the fault (downdip dimension). (b) Geometry of the bathymetry used in the tsunami simulations. The small bottom section with the gentlest slope closest to the shoreline is not shown in this figure because of the scale.

that additional factors adding to the variability is neglected in this study. Such factors may include the slip variation and rupture speed in the strike direction, bathymetry and topography effects, tidal variations, and finally two-dimensional wave phenomena such as refraction, reflection, focusing, and edge wave evolution.

2. Elastic Seabed Response to a Subduction Earthquake

2.1. Seabed Response to Coseismic Slip

[3] *Okada* [1985] derived analytical expressions for the surface displacement due to an inclined fault in a half-space for finite rectangular sources. These expressions have been broadly used to model ground surface deformations associated with earthquakes. In this study, we concentrate on interplate subduction events which are the most common source for large tsunamis observed around the world. We therefore limit our analysis to vertical displacement of the seabed due to pure dip slip on a reverse fault. *U* is taken as the movement of the hanging wall side block relative to the footwall side block (Figure 1). Considering pure dip slip only, we set strike and tensile components to zero. At the

seabed, the vertical permanent deformation u_z due to a dislocation along a surface in an isotropic elastic medium is given by *Okada* [1985, equation 26].

[4] In order to compute the vertical displacement due to a fault rupture with nonuniform slip distribution, we implement the *Okada* [1985] analytical solution for *n* equal elements with width *W/n* along the two-dimensional (2D) fault. We calculate and sum the local vertical displacements due to constant slip on each element, allowing for heterogeneous slip by varying *U* piecewise from segment to segment.

[5] The earthquake rupture process has for long been considered to follow a self-similar scaling relationship, since the stress drop has been observed to be independent of magnitude [*Aki*, 1967]. Earthquake self-similarity means that small earthquakes are not physically different from large earthquakes. Indeed, recent inversions of rupture mechanism have provided increasingly detailed slip distributions. *Mai and Beroza* [2000, 2002] analyzed published slip maps for different earthquakes to model mechanics of the rupture process. They derived a series of laws accounting for spatial complexity of earthquake slip along a fault plane. The authors proposed that the slip distribution follows an autocorrelation function only depending on the distance between
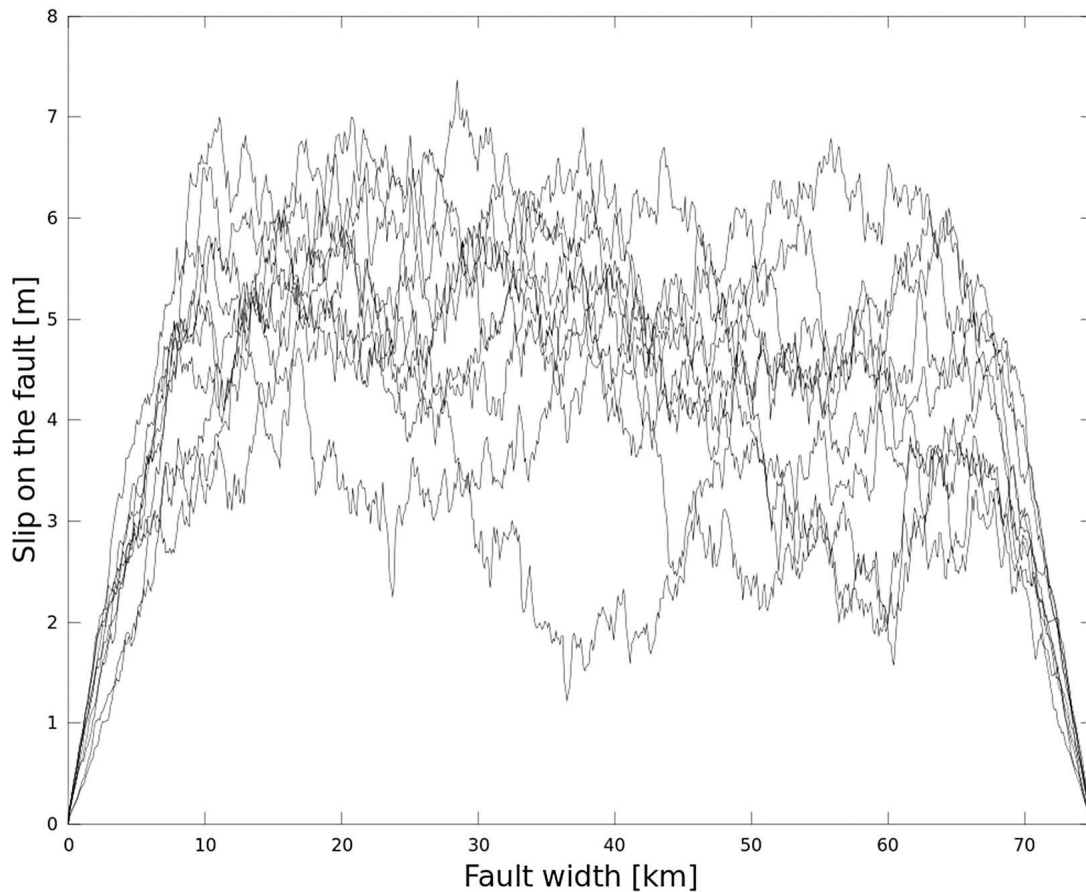
Figure 2. Example of a subset of the variable slip distributions used in the simulations.

two points on the fault plane and a downdip correlation length a. The correlation length can be derived from fault dimensions using $a \sim 1 + W/3$ where W is width (downdip dimension) of the fault in km. Among the possible autocorrelation functions, we chose to implement the exponential one that is characterized in space by $C(x) = e^{-x/a}$ and in the Fourier domain by the power spectrum $F(k) = 2a/(1 + a^2 k^2)$, where x is distance and k is wave number. The actual fluctuation of the slip is added to the mean slip by a multiplication of the spectral amplitude with a random phase term $e^{i\varphi(k)}$, subsequently transformed back to space using an inverse Fourier transformation. The fluctuation of slip is then scaled to 30% of the mean slip value of 5 m. The procedures for computing the distributed slip stochastically is adopted from *Roth and Korn* [1993].

[6] For this study, the fault width is set to 75 km, which leads to a correlation length a of 26 km. To be able to analyze the results stochastically, we generate 500 random slip distributions following the exponential autocorrelation function. For each rupture simulation, the slip value varies in the downdip direction and is tapered at the upper and lower edges of the fault. Examples of several randomly generated slip distributions are given in Figure 2.

2.2. Geometry and Seabed Displacements

[7] To design realistic trench topography, we use the continental slope along the Sumatra trench as a suitable

example. An average slope is computed along a section perpendicular to the subduction trench: 1:30 for Sumatra, with a nearshore slope of 1:39.5 at water depths less than 100 m. Outside of the trench, a constant ocean depth of 4000 m is assumed. The topography is shown in Figure 1. Naturally, the bathymetric profile affects the runup; a mild slope generally provides a larger amount of amplification than a steeper slope. Varying the slope of the bathymetric profile is beyond the scope of this paper.

[8] The fault segments are divided into $n = 746$ parts over the fault plane. Each of the 500 slip distributions is applied to the rectangular fault plane located along the plate interface. As we limit the study to plane wave propagation, we extract the solution in x-z space at the center of the fault plane. The dip angle δ is changed from 10° to 70°, and the depth of the upper edge h_m varies from 100 m to 30 km below the seabed. The shallowest depth of $h_m = 100$ m represents a rupture extending to the surface. However, it is necessary to place the fault at a certain depth to avoid mathematical singularities. In this particular case, the slip profile was not tapered at the upper edge of the fault. The results of the simulations for a limited number of realizations are plotted in Figure 3.

[9] The displacement due to a shallow dipping dip-slip event is very different from a steep fault event, which corresponds to the standard theory. For dip angles <30°, the initial seabed waveform is composed of a surface elevation
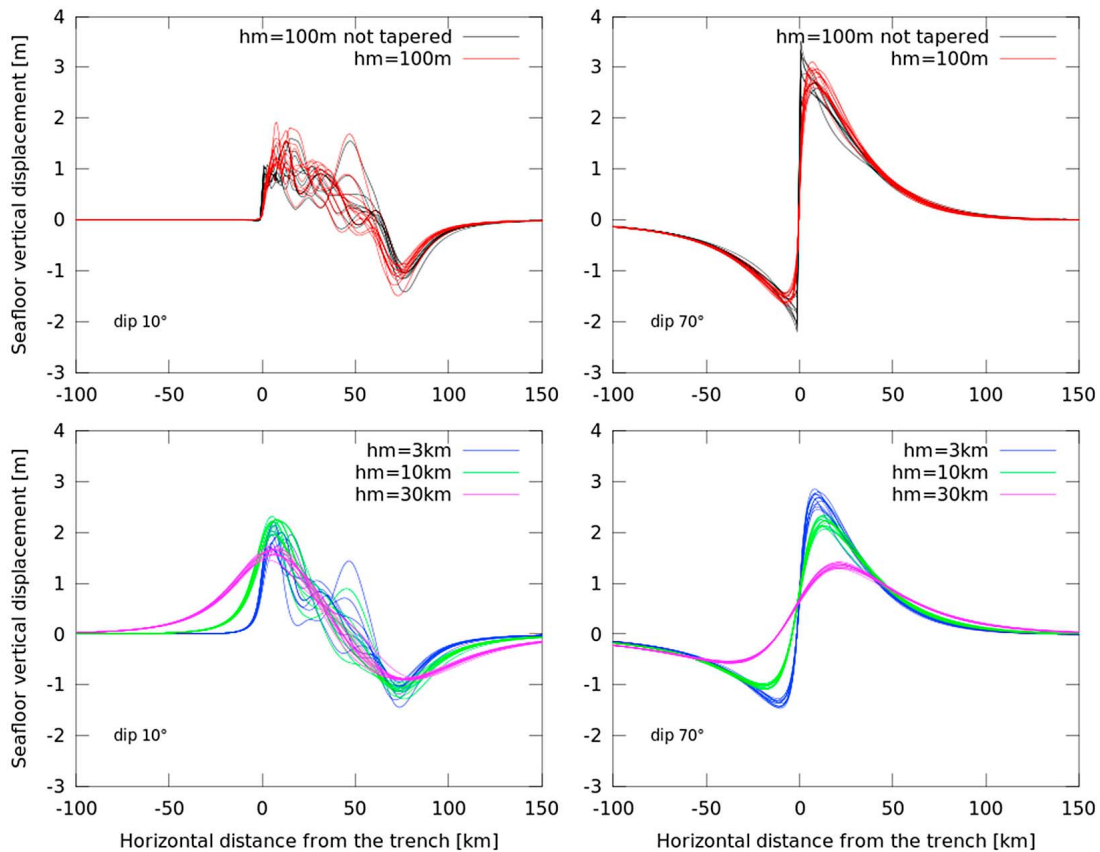
Figure 3. Permanent vertical displacement at the seabed due to thrust events with different fault geometries as a function of the distance from the trench for a subset of the realizations. Different colors are used for different fault depths h_m. We investigate two types of slip distributions for the subsurface fault ($h_m = 100$ m): the slip values are tapered (red lines) or not (black lines) at the upper edge. We observe a change in the wave polarity between dip angles shallower or steeper than $30°$. For clarity, we only present the two end-members of dip angles δ. (left) Shallow dipping fault with $\delta = 10°$, (right) steep fault $\delta = 70°$, (top) $h_m = 100$ m, and (bottom) $h_m = 3$, 10, 30 km.

flanked by a depression on its right. As a consequence, coasts located along the volcanic arc in the dip direction of the subduction zone (i.e., to the right of the x axis) will first observe a sea withdrawal. For steep faults (with dip angles >30°), the initial seabed waveform is composed of a depression followed by an elevation. As a consequence, coasts located along the volcanic arc in the dip direction of the subduction zone (i.e., to the right on the x axis) will only observe a small sea withdrawal, followed by a much larger increase in water level. We observe that for a thrust earthquake, the maximum predicted elevation is always larger than the maximum depression.

[10] In terms of runup estimation, we are interested in the maximum value of the vertical displacement and the total volume of water displaced. These two variables are analyzed with respect to their coefficient of variation (standard deviation σ divided by the mean μ). This coefficient displayed larger values in the cases of shallow rupturing and shallow dipping faults, whereas the imbedded faults and the faults with larger dip resulted in less variation (for brevity, the results are not displayed). A reduction of the coefficient of variation with increasing fault depth h_m was found, and is

interpreted as the depth acting as a low-pass filter on the seabed response.

3. Tsunami Propagation and Runup Estimation

3.1. Methodology

3.1.1. Initial Conditions for Tsunami Simulations

[11] Most tsunami models encountered in literature copy the seabed displacement directly from the seabed without taking the hydrodynamic response that filter out short-wave components at the seabed during tsunami generation into account. This approach may introduce nonphysical short wavelengths. To explore this issue, we therefore use both the seabed copied to the surface as well as modified seabed elevations as initial conditions in the subsequent tsunami simulations. Thus, we label the simulations using the seabed response directly as "copied," whereas the initial conditions modified due the hydrodynamic response are labeled "filtered." The methodology for quantifying the filtered initial water level is based on full potential wave theory. The method for filtering is derived from *Pedersen* [2001], and is similar to the model of *Kaijiura* [1963] applying a

hyperbolic cosine filter. The seabed uplift is instantaneous, and represented with piecewise constant values. The resulting initial water elevation represents the average elevation in the interval centered at each node.

3.1.2. Wave Propagation and Quantification of Runup in Large Ensembles

[12] Naturally, the crucial feature of a tsunami is its runup. A variety of approaches for nonlinear shoreline tracking has been attempted over the years; see for instance the review by *Pedersen* [2008a]. Today runup models are included in state of the art tsunami models based on the shallow water equations [*Titov and Synolakis*, 1995, 1998; *Imamura*, 1996; *LeVeque and George*, 2008; *Gayer et al.*, 2010], as well as in widespread coastal engineering codes based on Boussinesq type equations [e.g., *Kennedy et al.*, 2000; *Lynett et al.*, 2002; *Lynett*, 2006; *Son et al.*, 2011; *Zhou et al.*, 2011]. Still, in the present context where we need to perform several hundred thousands of simulations in a controlled and comparable manner, a simpler computational strategy is crucial.

[13] A few analytical solutions for runup on an inclined plane have been obtained by applying the hodograph transformation to the nonlinear shallow water equations, as first published by *Carrier and Greenspan* [1958] and later employed in a series of articles. However, the hodograph transformation essentially links the nonlinear problem to its linear counterpart, a wave equation with variable coefficients that still must be solved. This is generally obtained through the application of a Hankel transform, which put restrictions on the shape of the incident wave to obtain an explicit transformed waveshape. With a few notable exceptions, such as the asymptotic formula for solitary wave runup published by *Synolakis* [1987], the inverse transformation requires numerical integration. For our randomly generated initial conditions this kind of procedure is unsuitable. Fortunately, the analysis of runup based on the hodograph technique has also provided general and useful insight in the relation between linear and nonlinear shallow water solutions for runup. Provided that the incident wave is well described by linear theory, maximum runup and withdrawal are the same for the linear and the nonlinear description. On the other hand, the shoreline motion between these extreme values does depend on the nonlinearity. This is discussed by, for instance, *Synolakis* [1987] and, more elaborately, by *Didenkulova* [2009]. In the latter reference it is also demonstrated that other properties, e.g., the breaking limit, may be obtained from linear solutions. Breaking is here defined as a singularity in the hodograph transformation corresponding to a vanishing Jacobian determinant at the shoreline, implying that the surface elevation is becoming multivalued as a function of the horizontal coordinate. When the breaking criterion is expressed in terms of the vertical acceleration of the shoreline it reads [*Didenkulova*, 2009]

$$\gamma = \frac{1}{(\alpha^2 g)} \frac{\partial^2 \eta}{\partial t^2} = -\frac{1}{(\alpha g)} \frac{\partial u}{\partial t} > 1,$$

where α is the slope of the beach and the shoreline is to the left of the fluid. Implicit in the use of this criterion is the assumption that a bore will persist whenever breaking does occur. Hence, an incident wave that will produce breaking anywhere will also yield breaking at the shoreline. This is definitely the case within nonlinear shallow water theory. In

view of the geometry, which is two-dimensional and comprises a monotonous slope, this assumption is reasonable also from a physical point of view.

[14] As will be shown subsequently, dispersion may have a noticeable effect on the runup height. However, dispersion will be most important in the deep water part of the propagation [see *Pedersen*, 2008a] and we assume that the wave motion close to the shoreline is hydrostatic. Then, provided the dispersive deep water region and the nonlinear shallow water region do not overlap nonlinear, extreme shoreline excursions may again be obtained by linear theory. This is demonstrated by *Pedersen* [2008b] (benchmark 1). For waves that come close to breaking in finite depth dispersive effects may become important again, because of the steep wavefront, and lead to the evolution of undular bores that are sometimes observed for tsunamis [e.g., *Glimsdal et al.*, 2006; *Grue et al.*, 2008; *Madsen et al.*, 2008]. Undular bores are nonlinear and dispersive wave forms that are outside the framework of our modeling strategy that may be regarded as a combination of linear dispersive equations with nonlinear shallow water equations. Further, in the present investigation we are primarily concerned with nonbreaking runup heights or the occurrence of breaking of such. The first is presumably not affected by undular bores, while the breaking limits may be slightly modified, only, by dispersive effects at the shoreline.

[15] In the present article the topography is not represented by a single inclined plane, but by a broken plane joined to a deep sea region of constant depth. Still, as long as nonlinear effects are important only on the innermost slope leading to the shoreline, while dispersive effects then have become very small because of shoaling, both the breaking criterion and the linear values for the maximum runup will be valid. Again, it is emphasized that the general shoreline motion between the extreme values is not reproduced by linear theory, even though it can be derived from the linear time story of the shoreline [*Didenkulova*, 2009]. In the present filtered simulations, γ is in most cases less than unity during first runup (see Figure 4), implying validity of the employed linear theory. On the other hand, it should be noted that nonphysical breaking is frequent in the copied model runs for small dip angles and shallow rupture.

[16] In view of the discussion above we employ linear numerical models for the runup. We then solve the linear shallow water (LSW) equations, the linearized Boussinesq equations on standard form [*Peregrine*, 1967] and the linearized Nwogu formulation [*Nwogu*, 1993] that has better dispersion properties than the standard Boussinesq equations. To this end we employ a simple finite difference method with a staggered grid in space and time and centered differences. Further details on the method is found in work by *Løvholt and Pedersen* [2008], with the differential equations given in their equations 1–2 and Table 1, while the discretizations are defined in their equations 5–7 and Table 2. The extension to nonuniform grids is obtained simply by invoking the local grid increments in the discrete equations. Since the methods are linear, no tracing of the shoreline is needed. However, it is important that a velocity node is located at the shoreline, in which case no onshore extrapolation or fictitious nodes are needed. The runup performance of this method, for the LSW and standard Boussinesq equations, has been tested by *Pedersen* [2008b]
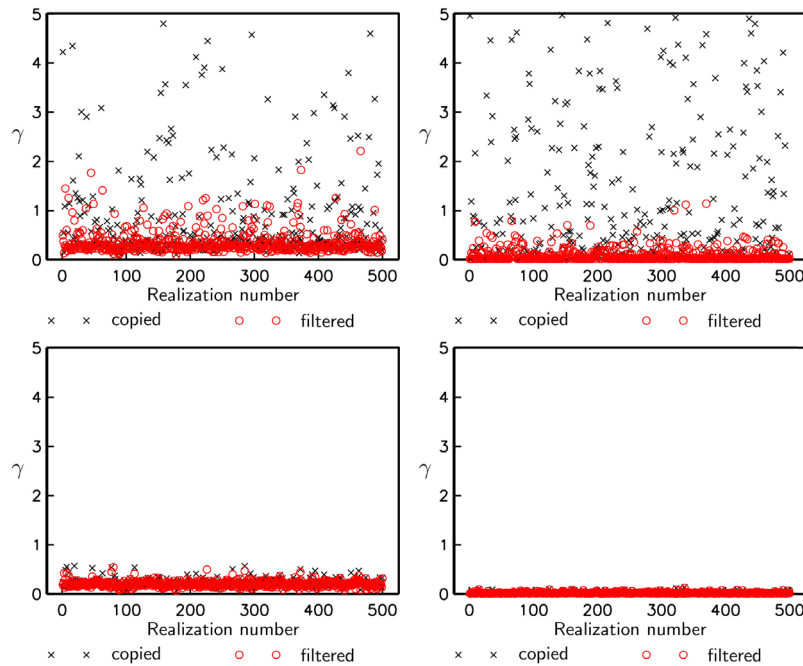
Figure 4. Breaking factor γ for all simulations on the shallow rupture geometry ($h_m = 100$ m) computed using the fluid acceleration at the shoreline. Crosses show the breaking factor for simulations using the seabed displacements as initial conditions, and circles show the breaking factor for simulations using the smoothed initial conditions. (top) Results for $10°$ dip and (bottom) results for $40°$ dip. (left) Results for the LSW simulations and (right) results for the dispersive (Nwogu) simulations.

and compared to fully nonlinear, Lagrangian models (NLSW, Boussinesq, full potential theory) with an accurate shoreline representation. For a benchmark test (numbered 1) it was found that the linear model reproduced the nonlinear maximum runup value very closely also for the Boussinesq equations, in accordance with the above discussion.

3.1.3. Grid Effects

[17] A variable grid is employed where the maximum grid increment at depths of 4000 m is Δx_{max}. Subsequently, the local Courant number is kept nearly constant at 0.9 until a given minimum water depth, H_{min} where a minimum spatial grid increment is employed, Δx_{min}. For water depths smaller than the threshold depth H_{min}, the grid increment remains equal to Δx_{min}.

[18] For each hydrodynamic model (LSW, standard linear dispersive, and linearized Nwogu; both copied and filtered initial elevation) and for each realization, minimum depth, and dip angle, simulations are conducted for three different grid resolutions, employing 500, 1000, and 2000 grid points. The finest resolution then corresponds to $\Delta x_{max} = 160$ m and $\Delta x_{min} = 5$ m. The convergence is evaluated on the ensemble level by computing the percentage error for mean values and standard deviations between the two finest resolutions. It is computed for each hydrodynamic model and parameter combination of δ and h_m. The largest relative error for the computed runup comparing the different grid resolutions is found for the LSW model with the copied initial conditions and a minimum fault depth of 100 m, ranging from 2.3% (for a $10°$ dip angle) to 3.1% (for a $70°$ dip angle) for the mean and 4.7% to 8.5% for the standard deviation. For the imbedded faults, and for all other combinations of initial conditions and models, errors were below 0.3% both for

the mean and the standard deviation, decreasing with increasing h_m.

3.2. Examples of Results From Single Realizations

[19] Figure 5 shows the initial water surface computed for $10°$ and $40°$ dip angles using the same slip realization at three different minimum depths h_m. For the case of shallow rupture, the difference between the filtered and copied initial conditions is distinct. For the $10°$ dip angle, short wavelength seabed undulations are clearly filtered on seabed response. In case of the $40°$ dip angle, the filtering results in a reduction in the peak of the initial water level and a gentler slope for the steep gradient located above the upper fault edge. However, the effect of filtering is small for the imbedded faults, and in the case of $h_m = 30$ km, the difference is barely visible.

[20] Figure 6 shows the simulated runup for the LSW model, using the water levels displayed in Figure 5 as initial conditions. As shown, the effect of filtering is most distinct for the shallow rupture. For $h_m = 100$ m, the difference between the two solutions (copied and filtered) is relatively limited during the first wave cycle. During the second wave cycle however, the corresponding solutions are distinctly different, and it is shown that the simulation using the copied initial condition overestimates the runup by about a factor 2 for the $10°$ case. The drawdown obtained for shallow rupture using the copied initial conditions largely exceeds the solution using the filtered initial condition. In fact, for most simulations breaking occurs during the drawdown after the first positive peak. This also holds for the dispersive simulations, see below for a discussion. Hence, the solution at later times may no longer be valid. For this reason, we
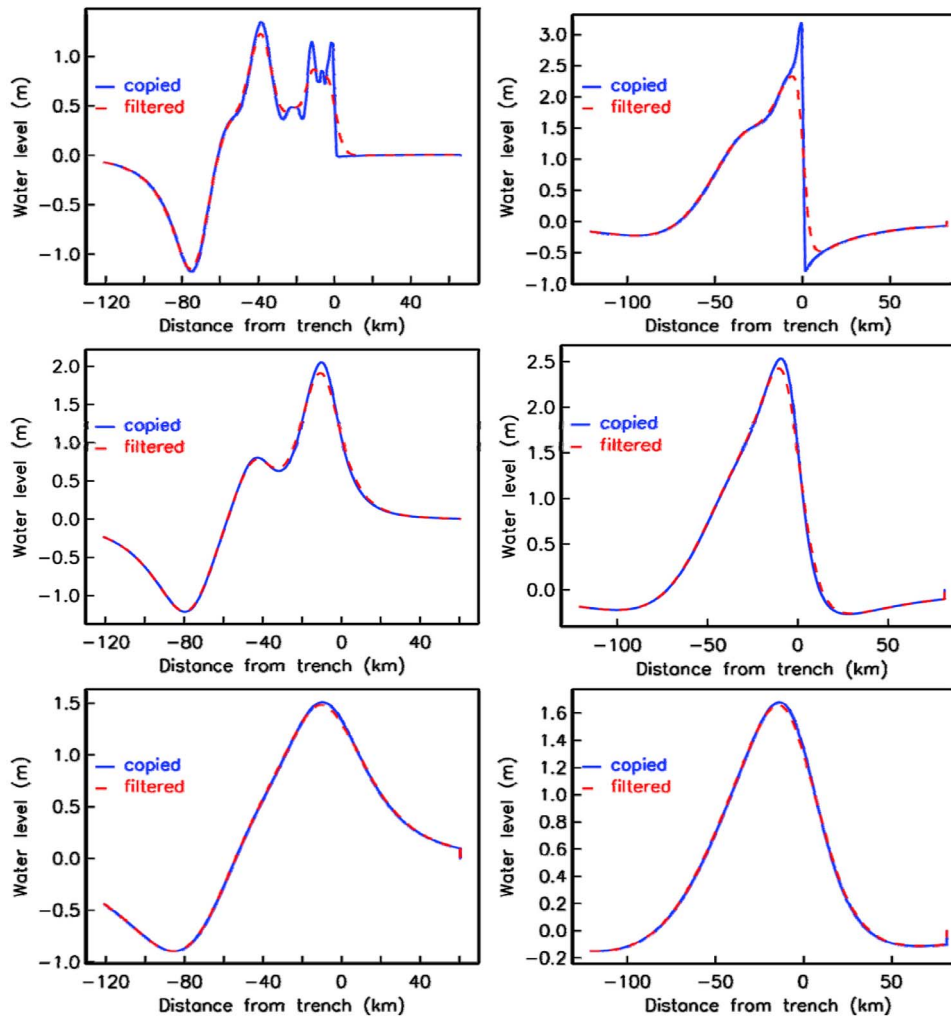
Figure 5. Comparison of the initial water surface obtained by copying the seabed displacement without filtering (solid curves) and with filtering (dashed curves) for six different realizations. Results for (top) $h_m = 100$ m, (middle) $h_m = 10$ km, and (bottom) $h_m = 30$ km. (left) Fault plane dip angle of $10°$; (right) fault plane dip angle of $40°$.

restricted subsequent analyses and statistics on the maximum runup to the first positive peak. We will claim that it still represents the maximum runup reasonably well, as the maximum runup arises within the first positive wave in most dispersive simulations. Given the small difference in initial conditions this relatively large overestimation in runup caused by the nonphysical short wavelengths may seem surprising. Nevertheless, this example demonstrates that even relatively small deviations due to artificial short wavelengths may contribute considerably to the runup or drawdown using a hydrostatic model.

3.3. Effects of Fault Parameters on the Maximum Runup

[21] We investigate the maximum runup for both the LSW and dispersive tsunami simulations for all shallow rupturing geometries and all realizations with respect to the fault parameters. Both copied and filtered initial conditions are used. We notice that comparing the higher-order dispersive model of *Nwogu* [1993] with a standard dispersive model

resulted only in negligible deviations. The effect of higher-order dispersion will hence not be addressed further.

[22] Figure 7 shows examples of the distributions of the simulated maximum runup with Poissonian and lognormal fits, established using built-in fitting functions in Matlab. The distributions are associated with a distinct skewness, enabling maximum runups markedly larger than the mean of the ensemble. The widest distributions are found for the LSW model with copied initial condition and a shallow rupture. The randomness of the runup is however clearly reduced by introducing dispersion, as the dispersive simulations show no extreme values such as the ones from the LSW model shown in Figures 7a and 7d. This is due to filtering of high-frequency components in the dispersive simulations during the arrival of the leading at the coastline. Submerging the fault to larger depths also reduces variability; moreover, the skewness of the maximum runup distribution is much less pronounced for imbedded faults.

[23] The mean value, standard deviations, and coefficient of variation of the maximum runup were computed for the different parameter and model combinations for the
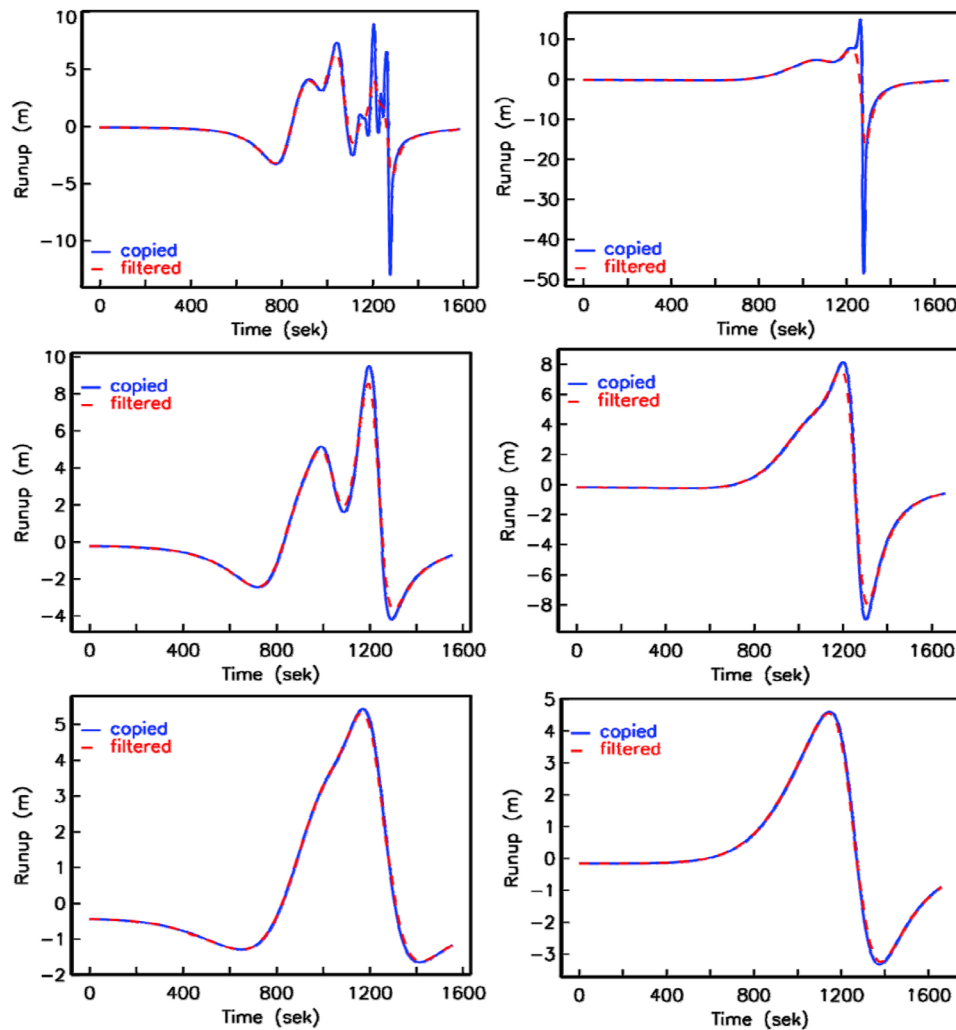
Figure 6. Simulated shoreline evolution as a function of time using the initial conditions shown in Figure 5. Simulations with initial water surface obtained by copying the seabed displacement without filtering (solid curves) and with filtering (dashed curves). Results for (top) $h_m = 100$ m, (middle) $h_m = 10$ km, and (bottom) $h_m = 30$ km. (left) Fault plane dip angle of $10°$; (right) fault plane dip angle of $40°$.

500 realizations. This statistic is presented below. To obtain a measure of the accuracy of the Monte Carlo simulation, we also computed the corresponding statistics for half subsets of the realizations. Deviations in the mean, the standard deviation and the coefficient of variation were typically found in the range of 1 to 5% comparing the sets with 250 and 500 realizations. Trends in these statistical outputs as functions of the different model parameters discussed below were not changed because of the finite number of realizations. It was therefore concluded that the 500 realizations were sufficient for this study, although a larger number of realizations would increase the accuracy. However, it is

noted that a similar number of realizations would be needed for generalization into two horizontal dimensions, which would enable the need for quite large computational resources.

[24] Figures 8a and 8b show mean value and standard deviation of the maximum runup as a function of the dip angle for the LSW and the dispersive model, respectively. For the LSW model, the effect of filtering the initial water level on the mean increases as a function of the dip. For the dispersive model, the effect of filtering is still clear, but more moderate and only pronounced for dip angles exceeding $40°$. Comparing Figures 8a and 8b we note that the standard

Figure 7. Distributions of maximum runup and fitted probability density functions. (a) LSW model with copied initial conditions for dip angle of $10°$ and a minimum depth of 100 m. (b) Nwogu model with filtered initial conditions for a dip angle of $10°$ and a minimum depth of 100 m. (c) LSW model with copied initial conditions for dip angle of $10°$ and a minimum depth of 30 km. (d) LSW model with copied initial conditions for dip angle of $40°$ and a minimum depth of 100 m. (e) Nwogu model with filtered initial conditions for a dip angle of $40°$ and a minimum depth of 100 m. (f) Nwogu model with copied initial conditions for dip angle of $40°$ and a minimum depth of 30 km.
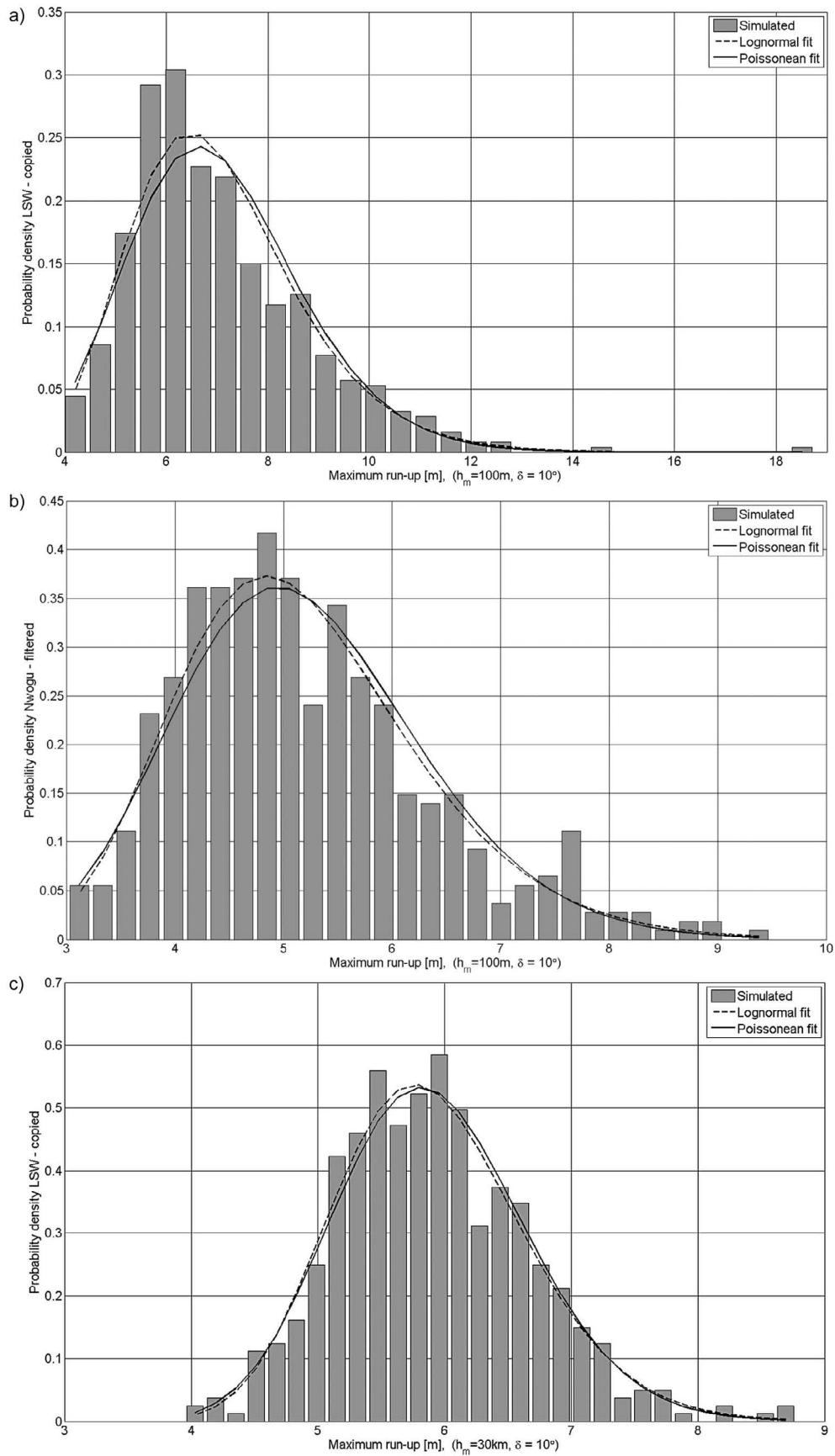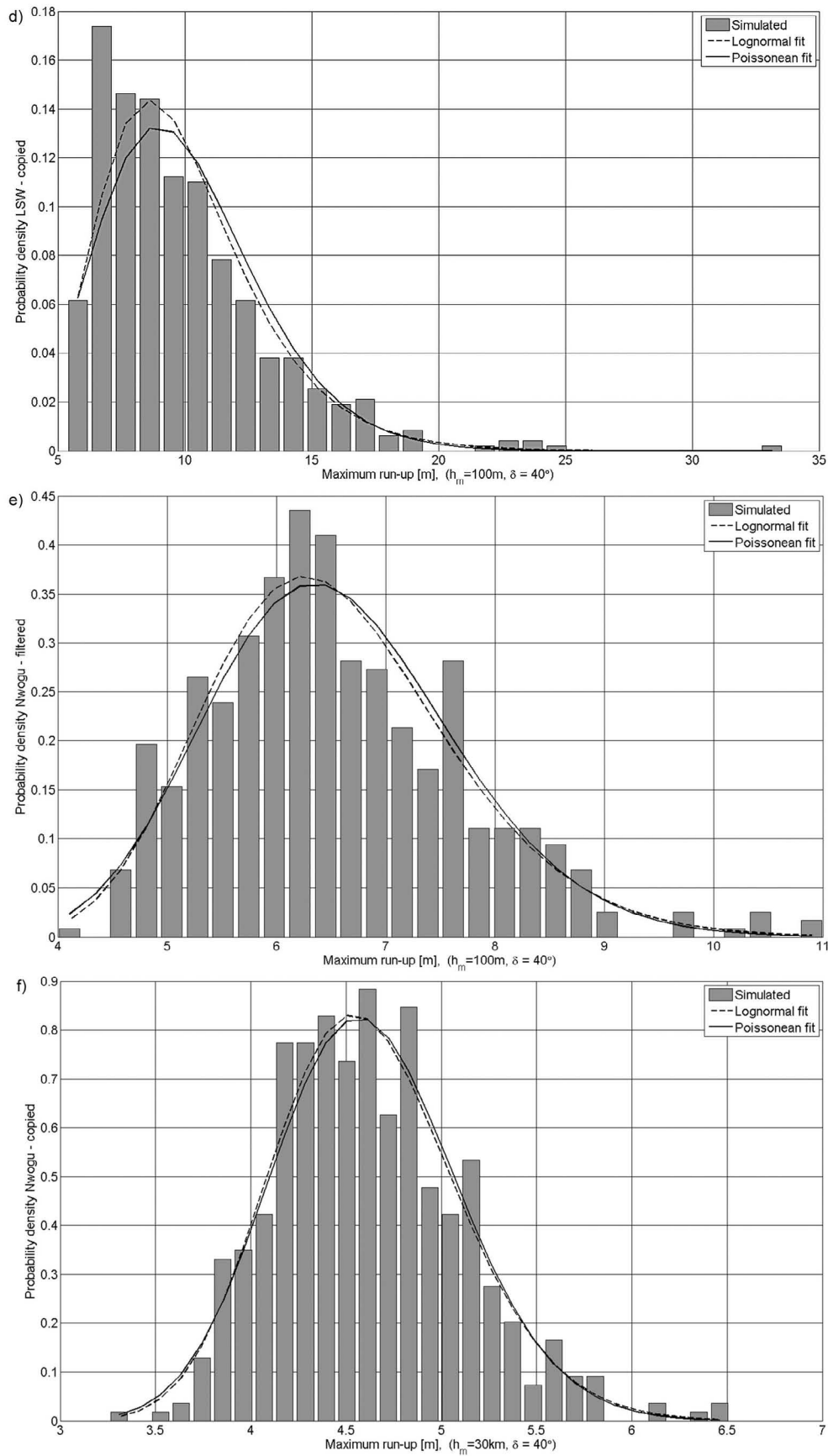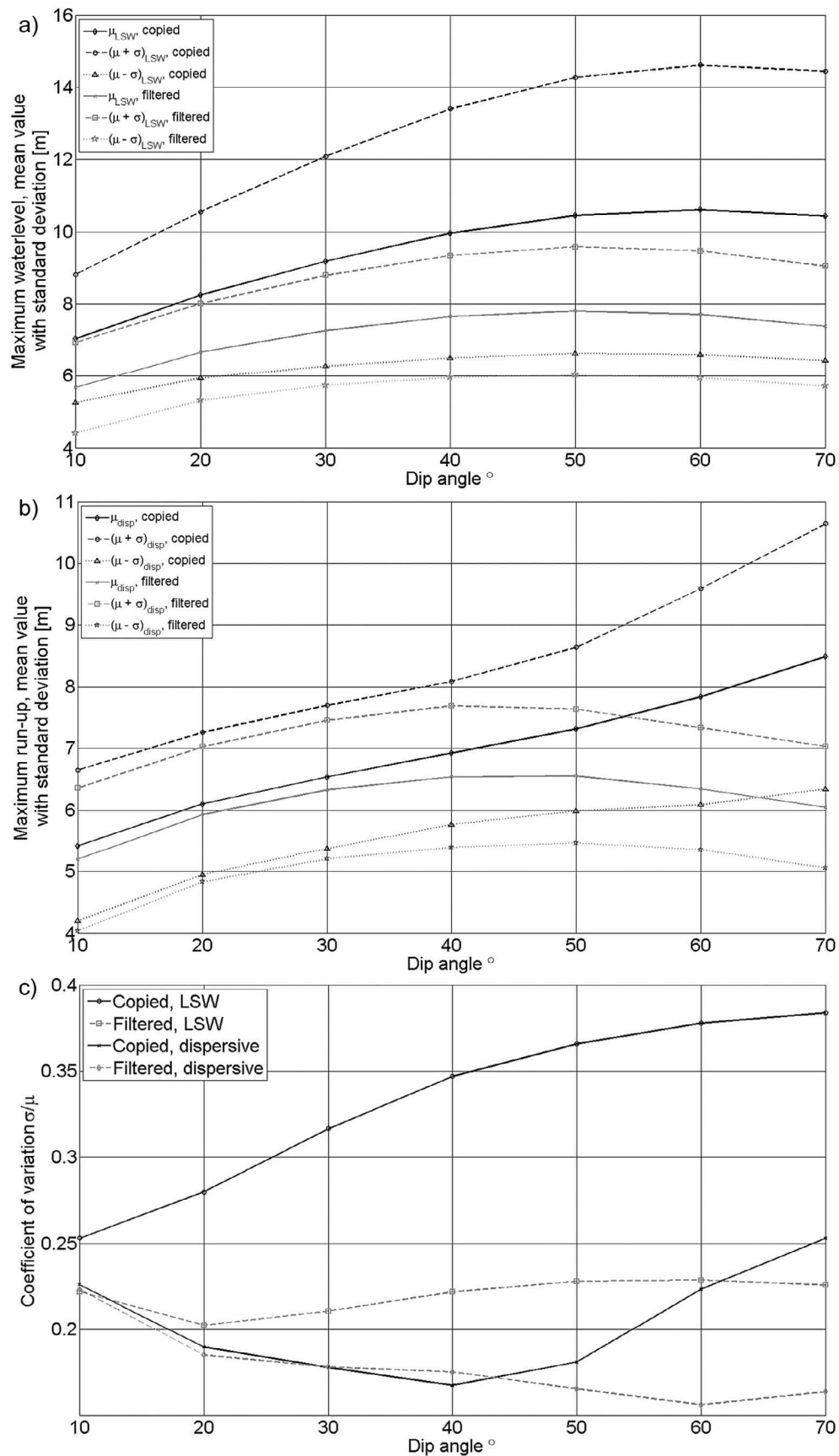
Figure 7

Figure 7. (continued)

Figure 8. Mean value of maximum runup including standard deviation as a function of dip angle for (a) the LSW model and for (b) the dispersive model; (c) coefficient of variation as a function of dip angle.
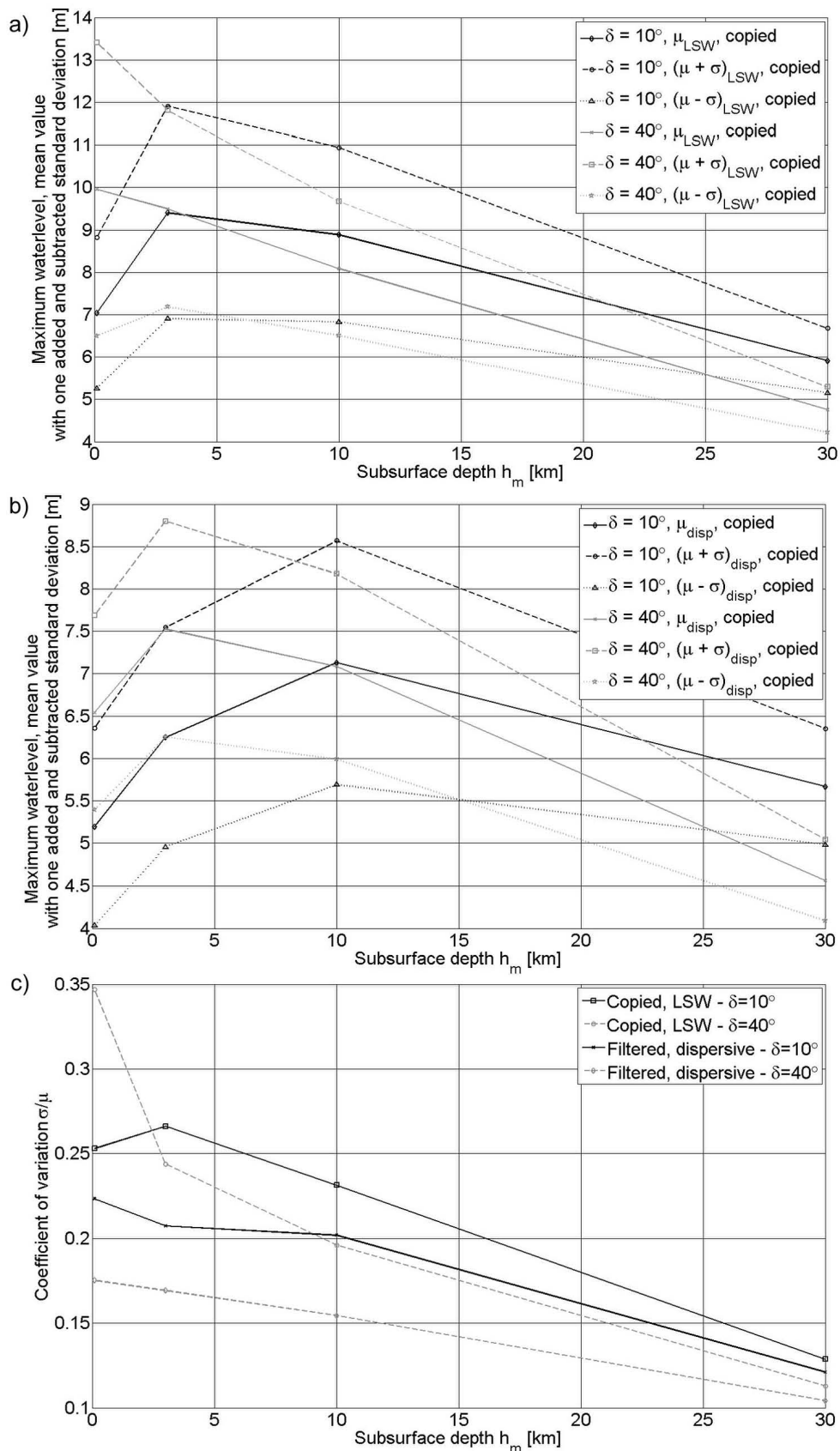
Figure 9. Mean value of maximum runup including standard deviation as function of the minimum fault depth for (a) the LSW model and for (b) the dispersive model; (c) coefficient of variation as function of the minimum fault depth.
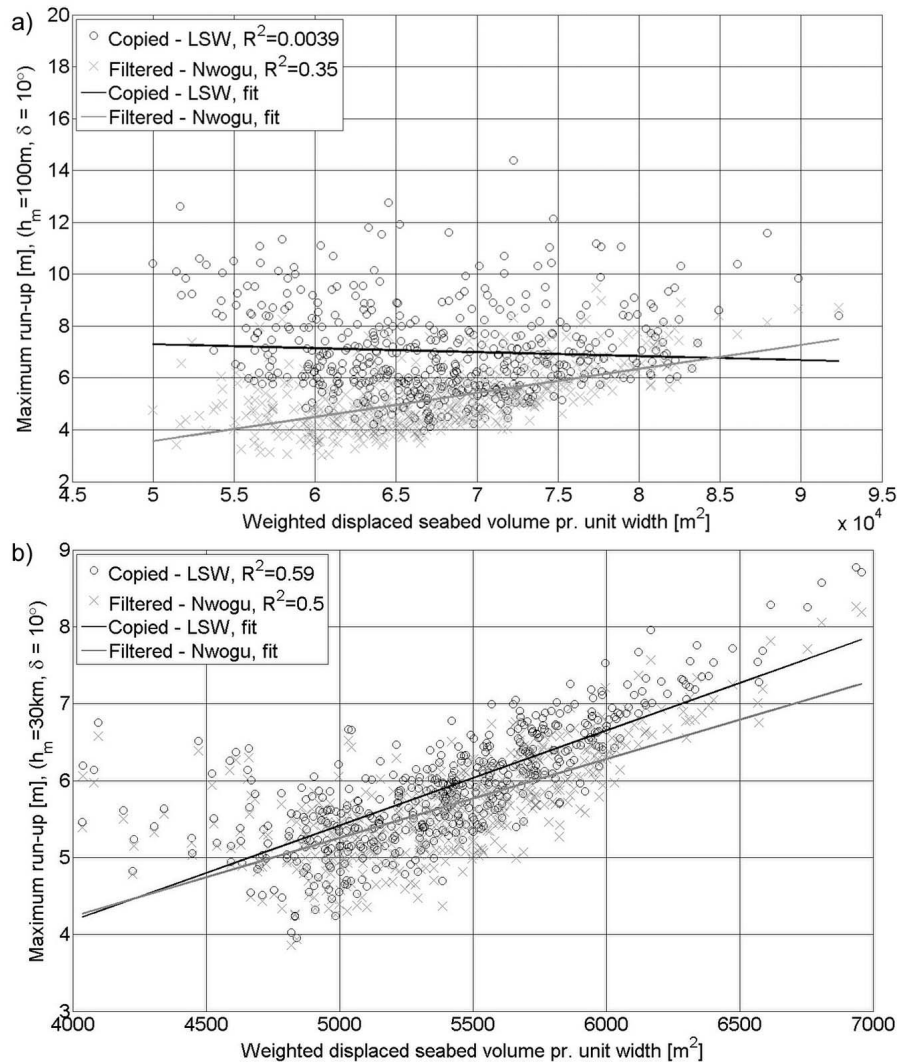
Figure 10. Maximum runup as a function of weighted displaced water volume for different minimum fault depths and dip angles. (a) Minimum fault depth of 100 m and 10° dip angle, (b) minimum fault depth of 30 km and 10° dip angle, (c) minimum fault depth of 100 m and 40° dip angle, and (d) minimum fault depth of 30 km and 40° dip angle.

deviation of the maximum runup is smaller for the dispersive model. The coefficient of variation is visualized in Figure 8c for the different combinations of initial conditions and models, showing clearly that filtering the initial water level reduces the variation of runup due to heterogeneous slip. It also shows that dispersion during propagation reduces the coefficient of variation. For the most general solution (filtered initial water level and usage of dispersive model), the coefficient of variation is decreasing as a function of the dip angle, i.e., the standard deviation is 22% of the mean for the 10° dip angle, compared to 16% for 70°.

[25] Figures 9a and 9b show mean value and standard deviation of the maximum runup as a function of the minimum fault depth for LSW and dispersive model, respectively. For shallow dip angles, the mean value first increases from $h_m = 100$ m to $h_m = 3$ km. A likely reason for this is the accumulation of localized strain close to the uppermost part

of the imbedded faults leading to increased seabed elevation close to the fault tip. This effect is most pronounced for dispersive simulations. For larger values of the minimum fault depth, the maximum runup decreases as expected. Figure 9c depicts the coefficient of variation, showing that the variability of the maximum runup decreases as a function of increasing minimum fault depth. This is interpreted as an effect of the imbedded faults acting as a low-pass filter on the surface displacement.

3.4. Maximum Runup Correlation With Seabed Response

[26] The different slip realizations result in a range of initial seabed responses. We investigate to which extent the simulated maximum runup was governed by the characteristics of the seabed displacements, by investigating different parameters.
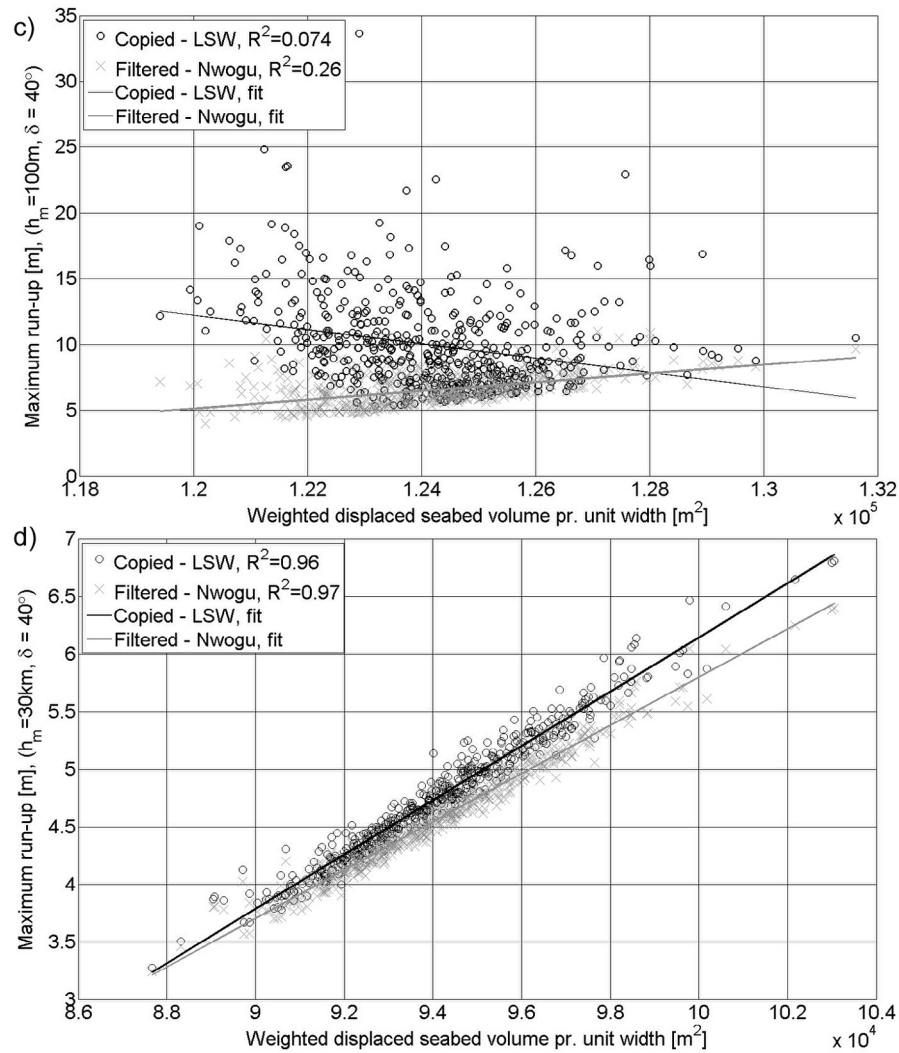
Figure 10. (continued)

[27] The first parameter is the integrated absolute seabed displacement times the 1/4 power of the absolute water depth H normalized by the maximum water depth $H_0 = 4500$ m, denoted weighted displaced water volume V_w below, i.e.,

$$V_w = \int |u_z(H)| \cdot (H/H_0)^{1/4} dx.$$

[28] The idea behind scaling with the water depth is to take into account the potential for amplification due to shoaling following Green's law, i.e., that wave components generated at larger depth amplify more. The maximum runup as a function of weighted displaced water volume is shown in Figure 10. For the shallow rupture ($h_m = 100$ m), the correlation is almost zero for the LSW model with copied initial water level, whereas somewhat more distinct for the dispersive simulations. For the imbedded faults, the correlation is improved, and a very good correspondence

with little variability is found when combined with the steepest dipping faults, as exemplified for $h_m = 30$ km in Figure 10.

[29] A second set of parameters comprises the maximum vertical seabed elevation, the maximum seabed depression, and the peak-to-peak vertical distance between these two quantities (mimicking roughly the maximum initial wave height). Of all these, the latter provides the best correlation. Figure 11 shows the maximum runup for all realizations as a function of the maximum peak-to-peak vertical seabed distance. Compared to the weighted volume, improved correlation is observed, also regarding the surface rupturing faults ($h_m = 100$ m). A possible explanation for the increased correlation for the peak-to-peak displacement compared to the weighted volume is that fluctuations in the surface elevation that contribute to the volume contribute less to the maximum runup. The peak-to-peak seabed displacement is therefore a better measure of the tsunamigenic potential than
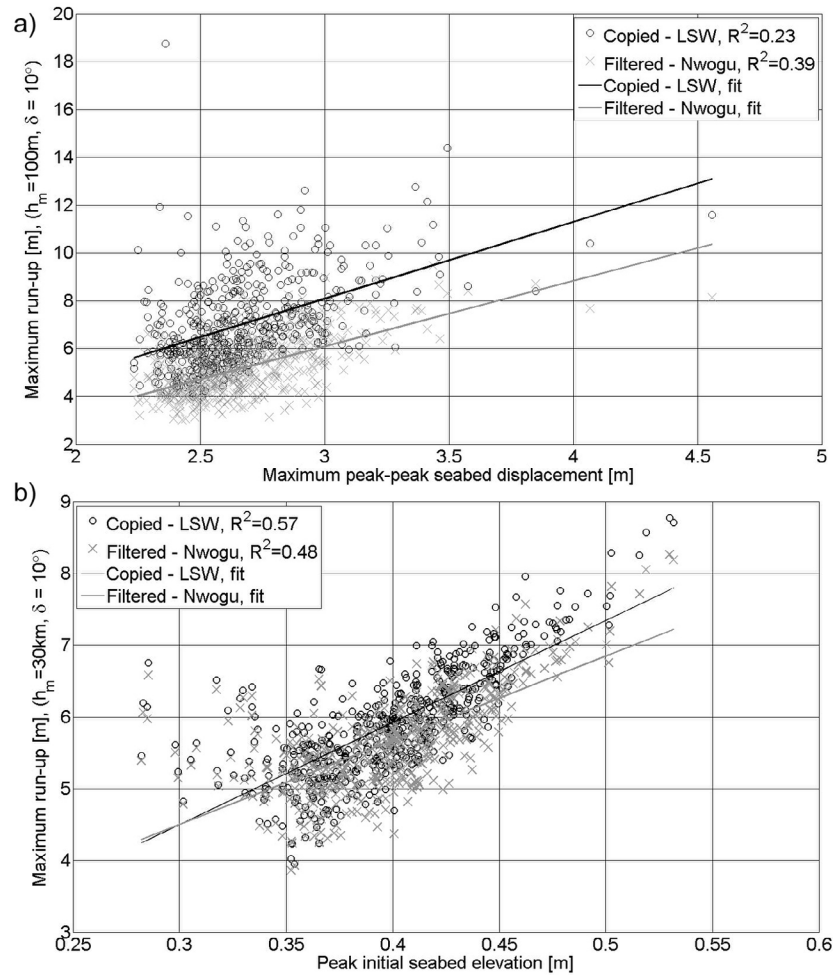
Figure 11. Maximum runup as function of peak-to-peak initial seabed displacement for different minimum fault depths and dip angles. (a) Minimum fault depth of 100 m and 10° dip angle, (b) minimum fault depth of 30 km and 10° dip angle, (c) minimum fault depth of 100 m and 40° dip angle, and (d) minimum fault depth of 30 km and 40° dip angle.

the weighted volume, particularly for shallow dip when displaced seabed fluctuations are prominent.

4. Concluding Remarks

[30] The purpose of this study is to quantify the effects of nonuniform coseismic slip in the dip direction on stochastic tsunami runup variability. We investigate tsunami generation and maximum runup due to subduction earthquakes with idealized geometries for a large number of numerical simulations by exploring the dependence of predicted tsunami heights on the heterogeneous coseismic slip distribution and dispersion. The seabed configurations are represented by a piecewise linear profile, and wave propagation is plane. The simplified geometry enables transparent results when varying fault and hydrodynamic properties compared to a more realistic topography. The dip angle varies from 10° to 70° and the fault depth from 100 m to 30 km. A total of 500 rupture realizations are modeled in each case.

[31] Seabed displacements are computed using a generalization of the *Okada* [1985] model. The sea surface response is either a direct copy of the seabed displacement, or

computed using the Green's function approach by *Pedersen* [2001]. A simple computational strategy using linear models was employed because of the need of performing several hundred thousand model runs. Correct values for maximum runup of nonbreaking waves, and breaking limits, may then be obtained as long as shoaling effects make dispersion very weak before nonlinearity starts to matter. By analyzing the breaking number given by *Didenkulova* [2009], we find that for most cases and for the first wave cycle, breaking does not occur for the current combination of fault, seabed, and slip configuration for dispersive simulations. The results obtained by dispersive wave models therefore resemble closely a "realistic" runup distribution.

[32] The current paper supports the conclusion of earlier studies on stochastic shoreline response due to earthquake tsunamis, suggesting large possible runup variations even for a given magnitude. Still, we find that there are various factors related to the wave generation and propagation that reduces the variability, and that not all of these factors are commonly applied. The coefficient of variation of the runup displays its largest values for shallow faults. Increasing fault depth is found to reduce the observed variability (in terms
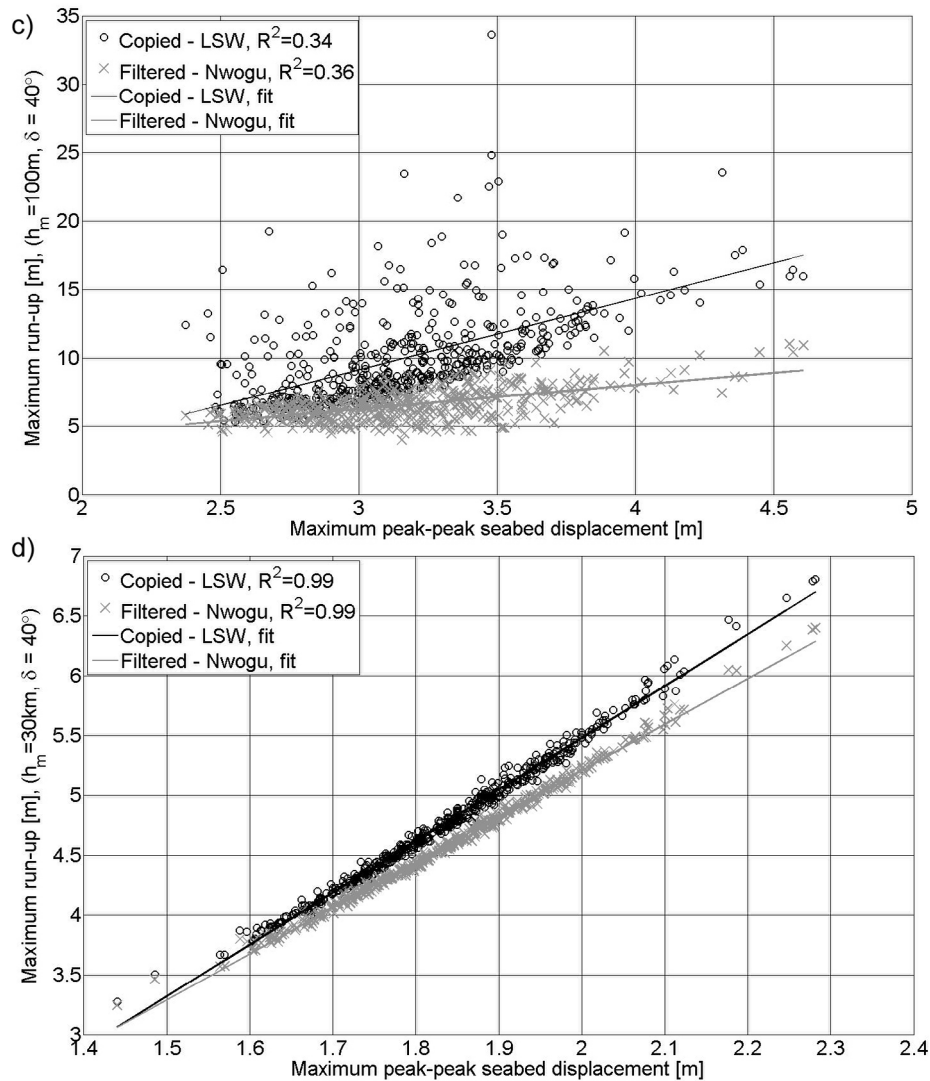
Figure 11. (continued)

of the coefficient of variation) of the seabed response. Frequency dispersion reduces the variability of the runup further, first by filtering high-frequency seabed undulations during tsunami generation, and second during the propagation phase. Shallow water models may therefore overestimate the maximum runup and its variation because of heterogeneity where such heterogeneities persist over a longer distance in the strike direction. Wave breaking may however reduce this variation to a certain extent. It is noted that by tuning the grid resolution in a shallow water model, numerical dispersion that mimics the dispersion curve may be obtained at a given water depth [see, e.g., *Shuto*, 1991]. However, for the current geometry with a considerable depth gradient; this strategy is not recommended.

[33] Furthermore, correlations between the maximum runup with various sets of seabed displacement parameters are sought. The best candidates found in this study are the scaled seabed volume per unit length and the maximum peak-to-peak vertical seabed displacement. For the deepest faults ($h_m = 30$ km), both parameters provide a strong correlation with the runup. Generally, the steepest dipping faults show better correlation than the shallow ones. For the shallow dipping faults, the peak-to-peak seabed displacement offers better correlation than the scaled seabed volume.

[34] The coefficient of variation varies between 16% and 22% for a surface rupturing earthquake in the configuration studied here. These are substantial variations, and points to the fact that stochastic effects should be taken into account in tsunami hazard mapping. However, the present case considers plane wave propagation and a uniform shoreline. Factors such as wave breaking and three-dimensional effects on the initial conditions and the shoreline configuration are believed to reduce the variability further as demonstrated by *Geist* [2002]. Hence, the current results should not be interpreted in absolute terms. On the other hand, the results highlight some fundamental effects that influence the variability of the maximum runup that previously have been neglected.

References

Aki, K. (1967), Scaling law of seismic spectrum, *J. Geophys. Res.*, *72*(4), 1217–1231, doi:10.1029/JZ072i004p01217.

Blaser, L., F. Krüger, M. Ohrnberger, and F. Scherbaum (2010), Scaling relations of earthquake source parameter estimates with special focus on subduction environment, *Bull. Seismol. Soc. Am.*, *100*, 2914–2926, doi:10.1785/0120100111.

Blaser, L., M. Ohrnberger, C. Riggelsen, A. Babeyko, and F. Scherbaum (2011), Bayesian networks for tsunami early warning, *Geophys. J. Int.*, *185*(3), 1431–1443, doi:10.1111/j.1365-246X.2011.05020.x.

Bolshakova, A., and M. Nosov (2011), Parameters of tsunami source versus earthquake magnitude, *Pure Appl. Geophys.*, *168*, 2023–2031, doi:10.1007/s00024-011-0285-3.

Carrier, G. F., and H. P. Greenspan (1958), Water waves of finite amplitude on a sloping beach, *J. Fluid Mech.*, *4*, 97–109, doi:10.1017/S0022112058000331.

Didenkulova, I. (2009), New trends in the analytical theory of long sea wave runup, in *Applied Wave Mathematics: Selected Topics in Solids, Fluids, and Mathematical Methods*, edited by E. Quak and T. Soomere, pp. 265–296, Springer, Berlin, doi:10.1007/978-3-642-00585-5_14.

Gayer, G., S. Leschka, I. Nöhren, O. Larsen, and H. Günther (2010), Tsunami inundation modelling based on detailed roughness maps of densely populated areas, *Nat. Hazards Earth Syst. Sci.*, *10*, 1679–1687, doi:10.5194/nhess-10-1679-2010.

Geist, E. L. (2002), Complex earthquake rupture and local tsunamis, *J. Geophys. Res.*, *107*(B5), 2086, doi:10.1029/2000JB000139.

Geist, E. L., and R. Dmowska (1999), Local tsunamis and distributed slip at the source, *Pure Appl. Geophys.*, *154*, 485–512, doi:10.1007/s000240050241.

Glimsdal, S., G. Pedersen, K. Atakan, C. Harbitz, H. P. Langtangen, and F. Løvholt (2006), Propagation of the Dec. 26, 2004 Indian Ocean tsunami: Effects of dispersion and source characteristics, *Int. J. Fluid Mech. Res.*, *33*(1), 15–43, doi:10.1615/InterJFluidMechRes.v33.i1.30.

Grue, J., E. N. Pelinovsky, D. Fructus, T. Talipova, and C. Kharif (2008), Formation of undular bores and solitary waves in the Strait of Malacca caused by the 26 December 2004 Indian Ocean tsunami, *J. Geophys. Res.*, *113*, C05008, doi:10.1029/2007JC004343.

Henry, C., and S. Das (2001), Aftershock zones of large shallow earthquakes: Fault dimensions, aftershock area expansion and scaling relations, *Geophys. J. Int.*, *147*, 272–293, doi:10.1046/j.1365-246X.2001.00522.x.

Imamura, F. (1996), Simulation of wave-packet propagation along sloping beach by TUNAMI-code, in *Long-Wave Runup Models*, edited by H. Yeh, P. L.-F. Liu, and C. Synolakis, pp. 231–241, World Sci., Singapore.

Kaijiura, K. (1963), The leading wave of a tsunami, *Bull. Earthquake Res. Inst. Univ. Tokyo*, *41*, 535–571.

Kennedy, A. B., Q. Chen, J. T. Kirby, and R. A. Dalrymple (2000), Boussinesq modeling of wave transformation, breaking, and runup. I: 1D, *J. Waterw. Port Coastal Ocean Eng.*, *126*(1), 39–47, doi:10.1061/(ASCE)0733-950X(2000)126:1(39).

Leonard, M. (2010), Earthquake fault scaling: Self-consistent relating of rupture length, width, average displacement, and moment release, *Bull. Seismol. Soc. Am.*, *100*, 1971–1988, doi:10.1785/0120090189.

LeVeque, R., and D. L. George (2008), High-resolution finite volume methods for the shallow water equations with bathymetry and dry states, in *Advanced Numerical Models for Simulating Tsunami Waves and Runup*, edited by P. L.-F. Liu, H. Yeh, and C. Synolakis, pp. 43–73, World Sci., Hackensack, N. J., doi:10.1142/9789812790910_0002.

Løvholt, F., and G. Pedersen (2008), Instabilities of Boussinesq models in non-uniform depth, *Int. J. Numer. Methods Fluids*, *61*, 606–637, doi:10.1002/fld.1968.

Løvholt, F., H. Bungum, C. B. Harbitz, S. Glimsdal, C. D. Lindholm, and G. Pedersen (2006), Earthquake related tsunami hazard along the western coast of Thailand, *Nat. Hazards Earth Syst. Sci.*, *6*, 979–997, doi:10.5194/nhess-6-979-2006.

Lynett, P. (2006), Nearshore wave modeling with high-order Boussinesq-type equations, *J. Waterw. Port. Coastal Ocean Eng.*, *132*, 348–357, doi:10.1061/(ASCE)0733-950X(2006)132:5(348).

Lynett, P. J., T.-R. Wu, and P. L.-F. Liu (2002), Modeling wave runup with depth-integrated equations, *Coastal Eng.*, *46*, 89–107, doi:10.1016/S0378-3839(02)00043-1.

Madsen, P. A., D. R. Fuhrman, and H. A. Schäffer (2008), On the solitary wave paradigm for tsunamis, *J. Geophys. Res.*, *113*, C12012, doi:10.1029/2008JC004932.

Mai, P. M., and G. C. Beroza (2000), Source scaling properties from finite-fault rupture models, *Bull. Seismol. Soc. Am.*, *90*, 604–615, doi:10.1785/0119990126.

Mai, P. M., and G. C. Beroza (2002), A spatial random field model to characterize complexity in earthquake slip, *J. Geophys. Res.*, *107*(B11), 2308, doi:10.1029/2001JB000588.

McCloskey, J., A. Antonioli, A. Piatanesi, K. Sieh, S. Steacy, S. Nalbant, M. Cocco, C. Giunchi, J. D. Huang, and P. Dunlop (2007), Near-field propagation of tsunamis from megathrust earthquakes, *Geophys. Res. Lett.*, *34*, L14316, doi:10.1029/2007GL030494.

McCloskey, J., A. Antonioli, A. Piatanesi, K. Sieh, S. Steacy, S. Nalbant, M. Cocco, C. Giunchi, J. D. Huang, and P. Dunlop (2008), Tsunami threat in the Indian Ocean from a megathrust earthquake west of Sumatra, *Earth Planet. Sci. Lett.*, *265*, 61–81, doi:10.1016/j.epsl.2007.09.034.

Nwogu, O. (1993), Alternative form of Boussinesq equations for nearshore wave propagation, *J. Waterw. Port Coastal Ocean Eng.*, *119*(6), 618–638, doi:10.1061/(ASCE)0733-950X(1993)119:6(618).

Okada, Y. (1985), Surface deformation due to shear and tensile faults in a half-space, *Bull. Seismol. Soc. Am.*, *75*, 1135–1154.

Pedersen, G. (2001), A note on tsunami generation by earthquakes [online], *Preprint Ser. Mech. Appl. Math.*, *4*, 1–8. [available at http://www.duo.uio.no/sok/work.html?WORKID=126788]

Pedersen, G. (2008a), Modeling runup with depth integrated equation models, in *Advanced Numerical Models for Simulating Tsunami Waves and Runup*, edited by P. L.-F. Liu, H. Yeh, and C. Synolakis, pp. 3–41, World Sci., Hackensack, N. J., doi:10.1142/9789812790910_0001.

Pedersen, G. (2008b), A Lagrangian model applied to runup problems, in *Advanced Numerical Models for Simulating Tsunami Waves and Runup*, edited by P. L.-F. Liu, H. Yeh, and C. Synolakis, pp. 311–315, World Sci., Hackensack, N. J., doi:10.1142/9789812790910_0017.

Peregrine, D. H. (1967), Long waves on a beach, *J. Fluid Mech.*, *27*, 815–827, doi:10.1017/S0022112067002605.

Roth, M., and M. Korn (1993), Single scattering theory versus numerical modelling in 2-D random media, *Geophys. J. Int.*, *112*, 124–140, doi:10.1111/j.1365-246X.1993.tb01442.x.

Shuto, N. (1991), Numerical simulation of tsunamis—Its present and near future, *Nat. Hazards*, *4*, 171–191, doi:10.1007/BF00162786.

Son, S., P. J. Lynett, and D.-H. Kim (2011), Nested and multi-physics modeling of tsunami evolution from generation to inundation, *Ocean Modell.*, *38*(1–2), 96–113, doi:10.1016/j.ocemod.2011.02.007.

Synolakis, C. E. (1987), The runup of solitary waves, *J. Fluid Mech.*, *185*, 523–545, doi:10.1017/S002211208700329X.

Titov, V. V., and C. E. Synolakis (1995), Modeling of breaking and non-breaking long-wave evolution and runup using VTCS-2, *J. Waterw. Port Coastal Ocean Eng.*, *121*(6), 308–316, doi:10.1061/(ASCE)0733-950X(1995)121:6(308).

Titov, V. V., and C. E. Synolakis (1998), Numerical modeling of tidal wave runup, *J. Waterw. Port Coastal Ocean Eng.*, *124*(4), 157–171, doi:10.1061/(ASCE)0733-950X(1998)124:4(157).

Wang, X., and P. L.-F. Liu (2006), An analysis of 2004 Sumatra earthquake fault plate mechanisms and Indian Ocean tsunami, *J. Hydraul. Res.*, *44*(2), 147–154, doi:10.1080/00221686.2006.9521671.

Wells, D. L., and K. J. Coppersmith (1994), New empirical relationships among magnitude, rupture length, rupture width, rupture area, and surface displacement, *Bull. Seismol. Soc. Am.*, *84*(4), 974–1002.

Zhou, H., C. W. Moore, Y. Wei, and V. V. Titov (2011), A nested-grid Boussinesq-type approach to modelling dispersive propagation and runup of landslide-generated tsunamis, *Nat. Hazards Earth Syst. Sci.*, *11*, 2677–2697, doi:10.5194/nhess-11-2677-2011.

S. Bazin, C. Harbitz, and F. Løvholt, NGI, PO Box 3930, Ullevål Stadion, N-0806 Oslo, Norway. (finn.lovholt@ngi.no; sara.bazin@ngi.no; carl.bonnevie.harbitz@ngi.no)

R. E. Bredesen, Simula Research Laboratory, PO Box 134, N-1325 Lysaker, Norway. (rolv@simula.no)

D. Kühn, International Center for Geohazards, c/o NGI, PO Box 3930, Ullevål Stadion, N-0806 Oslo, Norway. (daniela@norsar.no)

G. Pedersen, Department of Mathematics, University of Oslo, PO Box 1072, Blindern, N-0316 Oslo, Norway. (geirkp@math.uio.no)